



Resolving Atomistic Structure and Oxygen Evolution Activity in Nickel Antimonates

Journal:	<i>Journal of Materials Chemistry A</i>
Manuscript ID	TA-ART-11-2022-008854.R1
Article Type:	Paper
Date Submitted by the Author:	17-Dec-2022
Complete List of Authors:	<p>Kumar Rao, Karun; Stanford University, Chemical Engineering; SLAC National Accelerator Laboratory, SUNCAT Center for Interface Science and Catalysis; SLAC National Accelerator Laboratory, Liquid Sunlight Alliance</p> <p>Zhou, Lan; California Institute of Technology, Liquid Sunlight Alliance</p> <p>Lai, Yungchieh; California Institute of Technology, Liquid Sunlight Alliance</p> <p>Richter, Matthias; California Institute of Technology, Liquid Sunlight Alliance</p> <p>Li, Xiang; Lawrence Berkeley National Laboratory, Liquid Sunlight Alliance; SLAC National Accelerator Laboratory</p> <p>Lu, Yubing; Lawrence Berkeley National Laboratory, Molecular Biophysics and Integrated Bioimaging Division</p> <p>Yano, Junko ; Lawrence Berkeley National Laboratory, Liquid Sunlight Alliance; Lawrence Berkeley National Laboratory, Molecular Biophysics and Integrated Bioimaging Division</p> <p>Gregoire, John; California Institute of Technology, Liquid Sunlight Alliance</p> <p>Bajdich, Michal; SLAC National Accelerator Laboratory, SUNCAT Center for Interface Science and Catalysis; SLAC National Accelerator Laboratory, Liquid Sunlight Alliance</p>

Resolving Atomistic Structure and Oxygen Evolution Activity in Nickel Antimonates

Karun K. Rao,^{1,2} Lan Zhou,^{3,4} Yungchieh Lai,^{3,4} Matthias H. Richter,^{3,4} Xiang Li,^{5,6} Yubing Lu,⁷
Junko Yano,^{6,7} John M. Gregoire,^{3,4,*} Michal Bajdich^{1,**}

¹ SUNCAT Center for Interface Science and Catalysis and Liquid Sunlight Alliance, SLAC
National Accelerator Laboratory, Menlo Park, CA, USA

² Department of Chemical Engineering, Stanford University, Stanford, CA, USA

³ Division of Engineering and Applied Science, California Institute of Technology, Pasadena,
CA, USA

⁴ Liquid Sunlight Alliance, California Institute of Technology, Pasadena, CA 91125, USA

⁵ SLAC National Accelerator Laboratory, Menlo Park, CA 94025, USA

⁶ Liquid Sunlight Alliance, Lawrence Berkeley National Laboratory, Berkeley, CA 94720, USA

⁷ Molecular Biophysics and Integrated Bioimaging Division, Lawrence Berkeley National
Laboratory, Berkeley, CA 94720, USA

*E-mail (Exp.): gregoire@caltech.edu (J.M.G.) **E-mail (Theory): bajdich@slac.stanford.edu

(M.B.)

Abstract

The oxygen evolution reaction (OER) requires electrodes that are not only catalytically active, but also stable under harsh electrochemical environments to enable efficient, durable technologies. Our recent report of a stable amorphous $\text{Ni}_{0.5}\text{Sb}_{0.5}\text{O}_z$ OER photoanode established Ni-Sb-O as an important system for computational understanding of both the structural and catalytic behavior of

these complex oxides. In the present work we show that $\text{Ni}_x\text{Sb}_{1-x}\text{O}_z$ with $x > 0.33$ crystallizes into a previously unknown phase. Guided by experimental x-ray diffraction, we use density functional theory calculations to perform a prototype phase search to identify a broad family of stable and metastable mixed rutile and hexagonal-like phases for $x = 0.33, 0.50,$ and 0.66 compositions. For the identified phases, we predict favorable oxygen vacancy formation energies for Ni-rich compositions under the reducing synthesis conditions which match measured Ni K-edge x-ray absorption spectra. The calculated overpotential for the most active site decreases with increasing Ni content, from 0.91 V ($x = 0.33$) to 0.49 V ($x = 0.66$), which captures the experimentally observed trend. We find the active site changes from the Ni-O-Sb bridge to a Ni-O-Ni bridge at increasing Ni concentrations, rather than the commonly studied singly under-coordinated sites. Finally, detailed Pourbaix analysis of the identified phases show excellent electrochemical stability, consistent with experimentally measured low metal ion concentrations in the electrolyte of photoelectrochemical cells. Collectively, our consideration of an ensemble of structures enables identification of the most catalytically prolific structural motifs, aiding the understanding of crystalline and amorphous catalysts and elucidating the co-optimization of activity and durability in nickel antimonates.

Introduction

One strategy to economically reduce the amount of CO₂ in the atmosphere is solar photoelectrochemical generation of chemical fuels in which light, CO₂, and H₂O are converted into higher order hydrocarbons.¹ These hydrocarbons can either be used as fuels, chemical feedstocks, or permanently sequestered. One of the limiting factors preventing commercialization of such a device is the lack of a suitable photoanode for the oxygen evolution reaction (OER).² A suitable photoanode must not only have a low overpotential for the OER to improve overall efficiency, but also be durable enough to prevent corrosion or degradation under the highly oxidizing conditions.³ While many metal oxides have been studied as photoanodes, metal antimonates represent an interesting class of materials with excellent operational stability.

Recently, combining high throughput experimentation methods and theory, nickel-antimony oxides were investigated for photo-electrocatalysis of the OER.⁴ It was shown that an amorphous Ni_xSb_{1-x}O_z photoanode with a Ni cation ratio of $x = 0.5$ meets the requirements of operational stability, visible photo-response, and appreciable photovoltage. While the amorphous nature of this photoanode creates a new pathway for development of stable photoanodes that lack crystal anisotropy, the absence of a definite periodic bulk structure poses challenges for a direct computational study⁵.

Prior computational and experimental studies of transition metal-antimonides for oxygen reduction and evolution reactions have discussed trends in activity and electrochemical stability.⁶⁻⁹ However, experimentally, these studies generally synthesized crystalline stoichiometries of MSb₂O₆ ($x = 0.33$) and do not consider either antimony-poor ($x > 0.33$), or amorphous

compositions. In the present work, we discover that amorphous, Ni-rich antimonates crystallize above 700 °C into a phase with no existing prototype, demonstrating an insufficient understanding of phase behavior in this composition system. The prior computational studies on rutile antimonates considered only the pristine, OH-terminated, and O-terminated surfaces with only metal-ontop active sites, leaving a breadth of catalyst compositions, structures, surface terminations, and active sites unexplored. Furthermore, while the effects of oxygen vacancies were considered for rutile Mn-Sb-O systems¹⁰, oxygen vacancies have yet to be studied in the Ni-Sb-O system. Collectively, our new experimental findings and the limited knowledge of this system highlight the need for computational identification of (meta)stable atomic structures in this family of nickel antimonates, especially for Ni rich ($x > 0.33$) compositions.

A Ni-Sb-O composition library is annealed at high temperatures to crystallize the previously reported amorphous phase. Density functional theory (DFT) screening is used to identify symmetries and structural prototypes observed in the XRD data, and the overall bulk thermodynamic stability of candidate structures is evaluated under reaction conditions. The stability of oxygen vacancies is considered and their impact on the Ni oxidation state was verified by comparing simulated and measured X-ray adsorption spectroscopy (XAS). DFT analysis of the identified structures suggest Ni-O-Sb bridge site as active OER site, which were not considered in previous studies on metal antimonates. Both the overall electrochemical stability and calculated overpotential as a function of Ni metal ratio agrees with the experimental observations. Our combined experimental and theoretical characterization of the high temperature annealed Ni-Sb-O photoanode materials extends our understating of metal antimonate (photo)electrocatalysts and

provides a computational framework to study amorphous structures by generating families of representative crystal structures to calculate relevant properties.

Methodology

Experimental Methods

Composition Library Synthesis. Continuous composition libraries of $\text{Ni}_x\text{Sb}_{1-x}\text{O}_z$ were synthesized by reactive co-sputtering of Ni and Sb metal sources using 103 W and 55 W radio-frequency power supplies, respectively, at room temperature in a custom-designed combinatorial sputtering system.² The composition gradients were attained by positioning Ni and Sb sources in a non-confocal geometry. The deposition proceeded in mixed O_2 (0.9 mTorr) and Ar (5.1 mTorr) with 10^{-8} Torr base pressure and was followed by a post-deposition anneal in a Thermo Scientific box oven in flowing air at 700 °C. Two kinds of 4-inch diameter substrates were used: i) SiO_2/Si (170 nm thermal oxide served as a diffusion barrier) for phase identification, and ii) glass with a conductive $\text{SnO}_2:\text{F}$ (FTO) coating, which served as the electrical back contact to the film for OER (photo)electrochemical tests.

Composition and Structure Characterization. The $\text{Ni}_x\text{Sb}_{1-x}\text{O}_z$ metal oxide compositions were characterized by x-ray fluorescence (XRF) to obtain values of $x = \text{Ni} / (\text{Ni}+\text{Sb})$ with ca. 1 at.% relative uncertainty. The oxygen signal, and thus stoichiometry $z = \text{O} / (\text{Ni}+\text{Sb})$, is not detectable by XRF experiment. These measurements were performed using an EDAX Orbis Micro-XRF system with an x-ray beam approximately 2 mm in diameter. The Ni K and Sb L XRF peak intensities were extracted from the Orbis software and converted to normalized compositions using

the sensitivity factor for each element calibrated by commercial XRF calibration standards (Micromatter™).

The composition libraries were further characterized by x-ray diffraction (XRD) for bulk crystal structure and phase distribution. XRD was acquired using a Bruker DISCOVER D8 diffractometer with Cu K α radiation on a series of evenly spaced positions along the composition gradient. The diffraction images were collected using a 2D VÅNTEC-500 detector and integrated into 1D patterns using DIFFRAC.SUITE EVA software. Phase identification proceeded by identifying candidates in the International Crystallography Diffraction Database (ICDD) that best match the integrated 1D XRD patterns.

XAS Measurements. XAS at Ni K-edge and Sb K-edge were measured at beamline 7-3 of Stanford Synchrotron Radiation Light source ([SLAC], CA, USA). The intensity of the incident X-rays was monitored using an Ar-filled ion chamber (Sb K-edge) and an N₂-filled ion chamber (Ni K-edge). The Ni_xSb_{1-x}O_z samples were measured in fluorescence mode using a 30-element Ge detector (Canberra). An Sb foil and a Ni foil were used for XAS energy calibration. The first inflexion point of the Ni foil spectrum and Sb foil spectrum were calibrated to 8333.0 and 30491.0 eV. The data for Ni_xSb_{1-x}O_z was recorded in continuous scan mode.

TEM Characterization. An FEI DualBeam focused ion beam/scanning electroscoppe was used to prepare a cross-sectional TEM specimen in the specific region tested for photoelectrochemical measurement. TEM experiments were carried out in an FEI Tecnai Osiris FEG/TEM instrument operated at 200 kV in bright-field mode. Selected area electron diffraction (SAED) patterns were taken using the same machine. The energy-dispersive x-ray spectroscopy (EDX) elemental

mapping was acquired using Bruker Quantax. This characterization was performed by Eurofins EAG Precision TEM in Santa Clara, California.

OER Catalytic Measurements. The OER performance of the $\text{Ni}_x\text{Sb}_{1-x}\text{O}_z$ catalysts (deposited on FTO/XG glass and annealed at 700 °C) and a NiO catalyst (deposited on FTO glass and annealed at 610 °C) was evaluated using a previously reported scanning droplet cell¹¹ (SDC) with flowing O_2 -saturated pH 10 aqueous electrolyte (0.1 M boric acid with 0.085 M potassium hydroxide and 0.25 M sodium sulfate, pH adjusted to 9.76, referred to as pH 10). The 3-electrode cell includes a Pt counter electrode, Ag/AgCl reference electrode, Gamry G 300 potentiostat, and custom LabVIEW software. Each selected $\text{Ni}_x\text{Sb}_{1-x}\text{O}_z$ composition was characterized by 3 steps: i) a slow cyclic voltammetry (CV) from 1.23 to 1.73 V and back to 1.23 V vs RHE at a scan rate of 0.01 V s^{-1} ; ii) a chronoamperometry (CA) measurement at 1.73 V vs RHE for 10 s; then iii) a two fast CV cycles between 0.73 V to 2.23 V vs RHE at a scan rate of 0.05 V s^{-1} . A droplet contact area of approximately 0.02 cm^2 was used for calculation of current density. The overpotential at 10 mA cm^{-2} for each composition was obtained from the last CV cycle.

OER Photoelectrochemistry Measurements. PEC measurements were performed with toggled LED illuminations in an aqueous pH 10 borate-buffered electrolyte with 0.1 M sodium sulfite as the sacrificial hole acceptor. Four sequential CA were measured at 1.23 V vs RHE under a series of 4 LEDs from 3.2 to 2.1 eV, immediately followed by a CV under 3.2 eV LED starting from 1.23 V vs RHE with a cathodic sweep and an anodic sweep back to 1.73 V vs RHE at a rate of 0.02 V s^{-1} .

Theoretical Methods

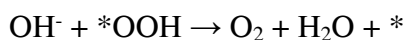
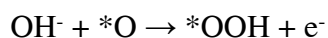
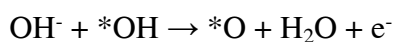
Electronic Structure Calculations. First-principles, spin-polarized, electronic structure calculations were performed using density functional theory (DFT) in the plane-wave basis and with projector augmented wave (PAW) pseudopotentials as implemented in the Vienna ab-initio simulation package (VASP)^{12,13}. For Antimony, a pseudopotential with explicit *d* electrons was chosen, Sb_GW(5s²4d¹⁰5p³). Calculations were performed with the PBE functional with a Hubbard U correction term^{14,15} optimized on experimental bulk formation enthalpies to 3.0 eV to account for on-site localization of Nickel *d*-electrons. For bulk geometry optimization, the plane wave energy cut-off was 600 eV, and the force convergence was 0.02 eV / Å, and a gamma-centered k-points grid of 25 / Å was used. Surface slabs were generated using the DFT-optimized bulk lattice constants with two fixed layers, two free layers, and 20 Å of vacuum, and were relaxed using the 500 eV wave energy cut-off and 0.02 eV / Å force convergence criteria.

XAS simulations. The FEFF9 program¹⁶ was used for the *ab initio* calculation of K-edge X-ray absorption near edge spectra (XANES) for Ni from DFT optimized structures. The adsorbing Ni atom was placed in the center of a cluster with radius of 10 Å. Simulation settings were chosen consistently with recent benchmarking work against experimental spectra¹⁷ and those used in the Materials Project³. Calculated spectra intensities were averaged over all symmetrically distinct Ni atoms, with gaussian smearing ($\sigma = 0.01$), and linearly scaled so the intensity of the first peak was 1.5.

Surface Pourbaix and OER Overpotential Calculations. The surface Pourbaix diagrams were constructed from free energies of H₂O, H₂, *OOH, *OH, and *O intermediates on RHE scales as

used previously.² The Gibbs free energies included a room temperature correction, zero-point energy, vibrational enthalpy, and entropic contributions as calculated using the harmonic oscillator approximation.

The OER thermodynamics was computed based on the following elementary steps in single site mechanism via OOH* under alkaline conditions¹⁸:



The theoretical overpotential is given by,

$$\eta (V) = \max[\Delta G_{* \text{OH}}, \Delta G_{* \text{O}} - \Delta G_{* \text{OH}}, \Delta G_{* \text{OOH}} - \Delta G_{* \text{O}}, 4.92 eV - \Delta G_{* \text{OOH}}] / e^- - 1.23V$$

where the adsorption energy of each intermediate is calculated from DFT on the most active surface calculated from the surface Pourbaix Diagram¹⁹, and the energetics of the coupled proton and electron is given from the computational hydrogen electrode scheme¹⁸.

Bulk Pourbaix Calculations. The bulk Pourbaix diagram was generated using the Pourbaix module in Pymatgen^{20,21}. To construct the diagram, experimental energetics were used for ionic species and the calculated free energy of formation of all solid-state phases included zero-point energy and entropy contributions. Each metal ion concentration was set to 10^{-6} M.

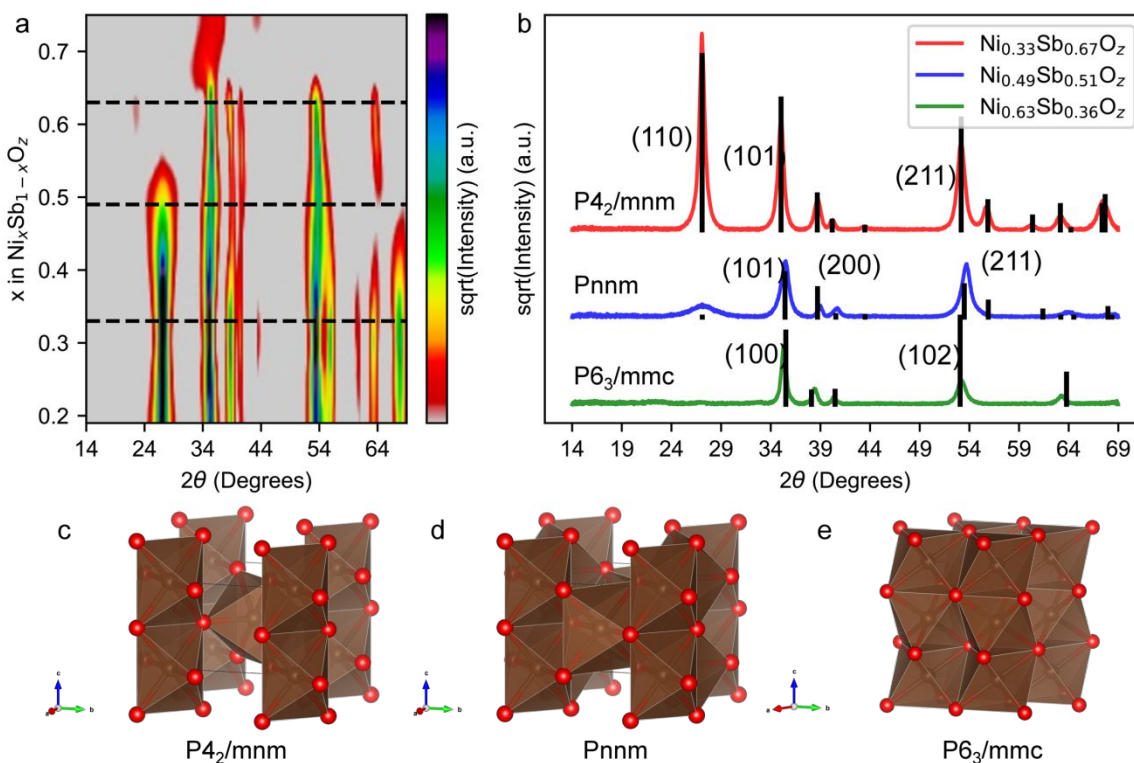


Figure 1: (a) The 2D XRD heatmap constructed from a series of 21 XRD patterns along the composition gradient of the Ni_xSb_{1-x}O_z library. This composition library was deposited on SiO₂/Si substrate with Ni concentration x from 0.19 to 0.75 and subsequently annealed at 700 °C in air. The three horizontal dashed lines mark compositions of interest of $x = 0.33, 0.49,$ and $0.63,$ where the latter 2 compositions contain XRD signals that do not correspond to known Ni-Sb-O phases. (b) The XRD patterns of these three compositions are shown with calculated XRD stick patterns from the disordered prototype crystal structures that were identified from the XRD-guided structure search. These structures have space groups of (c) P₄₂/mnm (rutile), (d) Pnmm, and (e) P₆₃/mmc (hexagonal) aligned with the $x = 0.33, 0.49$ and 0.63 spectra, respectively. In (c), (d), and (e), red circles are oxygen atoms and brown atoms/polyhedra are metal sites. The P₄₂/mnm. phase has metal site occupation of Ni_xSb_(1-x), while the proposed Pnmm and P₆₃/mmc prototypes have 50% vacancy on each metal site resulting in Ni_{x/2}Sb_{(1-x)/2} occupations.

Results

XRD Analysis and Prototype Identification

Figure 1a shows the XRD heatmap²² for the Ni-Sb-O composition library on SiO₂/Si annealed at 700 °C in 0.2 atm O₂. The examples of raw XRD images of samples in Figure 1a and 1b are shown in Figure S1, where uniform intensity diffraction rings indicate an equi-axed, powder-like crystallite distribution within the thin film samples, and the major peaks and their positions do not depend on the support. We refer to the experimentally synthesized compositions with the convention Ni_xSb_{1-x}O_z, where $x = \text{Ni}/(\text{Ni}+\text{Sb})$ indicates the Ni metal ratio and $z = \text{O}/(\text{Ni}+\text{Sb})$ represents the oxygen stoichiometry. At the composition $x = 0.33$, the diffraction peaks are well explained by a cation-disordered rutile Ni_{0.33}Sb_{0.66}O₂ prototype (Figure 1c) with space group P4₂/mmn and fitted lattice constants of $a = b = 4.662 \text{ \AA}$ and $c = 3.068 \text{ \AA}$. For $x > 0.72$, a weak NiO signal is observed. At intermediate compositions, $0.33 < x < 0.65$, the samples crystallize into phase(s) whose XRD patterns are unknown (no matches when searching in the ICDD database). When the same composition library is annealed at a lower temperature of 610 °C, the $x = 0.33$ composition crystallizes into the same cation-disordered rutile P4₂/mmn prototype, while compositions with $0.33 < x < 0.5$ partially crystallize into this prototype, and compositions with $0.5 < x < 0.65$ remain amorphous (Figure S2), demonstrating the new phase(s) exhibit a crystallization temperature between 610 and 700 °C.³

We make two observations in these spectra which support the claim of a new phase. Firstly, compared to the XRD pattern of $x = 0.33$ (Figure 1b red line) of the cation-disordered rutile prototype Ni_{0.33}Sb_{0.66}O₂, the (110), (210), (220), and (002) peak intensities are partially or completely suppressed in the spectra for $x = 0.49$ and 0.63 (Figure 1b blue and green lines). Suppression of the (110) diffraction peak intensity cannot be explained by a preferred crystalline

growth axis along a perpendicular direction (e.g., preferred growth along the (001) direction) which would result in suppression of comparable diffractions peaks such as (211), which is not observed. The suppression of diffraction intensity at 27° is thus intrinsic to either the form or structure factor of an unknown phase. Secondly, the peaks from the cation-disordered rutile $P4_2/mnm$ structure shift in this range, which could result from the overlap with the new unknown phase, indicating that the new phase(s) forms for all compositions x between 0.33 and 0.67. Additionally, the peaks of the unknown phase(s) appear to shift to lower 2θ (higher d -spacing) for $x > 0.52$, suggesting the new phase(s) support a range of cation stoichiometries.

To identify the new phase discovered by this combinatorial XRD study, we conducted a search of space group prototypes starting from known phases from Ni-Sb-O and related antimonate systems. Cation-disordered rutile prototype (Figure 1c) is composed of an oxygen sublattice with space group $P4_2/mnm$ and a disordered metal cation sublattice with space group $I4/mmm$ and fractional occupation $Ni_xSb_{(1-x)}$. XRD peaks at 38° and 40° are caused by scattering from the oxygen anion sublattice and are experimentally conserved at increasing Ni concentrations. Other peaks involving scattering from the cation sublattice, such as the (110) peak at 27° for $x > 0.5$ are suppressed in intensity. These two observations lead us to propose new structures that maintain the oxygen sublattice of the rutile structure while altering the cation sublattice space group. By invoking the $Cmmm$ space group for the cation sublattice, the prototype structure is orthorhombic with space group $Pnmm$ (Figure 1d). Compared to the disordered rutile cation sublattice with two metal sites, the $Pnmm$ prototype introduces two additional sites at the (0.5, 0, 0) and (0, 0.5, 0.5) interstitial positions and the occupation of all cation sites changes to $Ni_{x/2}Sb_{(1-x)/2}$ with 50%

vacancy. Adding these cations results in destructive interference of scattering along the (110) plane due to glide symmetry²³, which eliminates the peak at 27° while unaffected the other peaks. Fitting the lattice parameters of the Pnnm prototype to the $x = 0.49$ XRD pattern ($a = b = 4.652 \text{ \AA}$, $c = 3.02 \text{ \AA}$) shows excellent alignment between the predicted and observed peaks.

In addition to the Pnnm prototype, we find the oxygen anion sublattice of the β -Ni(OH)₂ layered structure (space group P6₃/mmc) also generates oxygen scattering peaks at 38° and 42°. The β -Ni(OH)₂ cation sublattice has one cation at the (0, 0, 0) position, is in space group P6/mmm, and generates a strong XRD peak at 19° due to the (001) plane. Following a similar procedure as above, we consider adding a cation in the (0, 0, 0.5) position which maintains the overall cation sublattice space group P6₃/mmc and causes destructive interference in the (001) direction, eliminating the intensity of the 19° peak (Figure S3). To maintain an overall density comparable to disordered rutile and β -Ni(OH)₂, the occupation of both cation sites again is set to Ni _{$x/2$} Sb _{$(1-x)/2$} with 50% cation vacancy (Figure 1e). Fitting lattice constants of the P6₃/mmc prototype to the $x = 0.63$ spectra ($a = b = 2.91 \text{ \AA}$, $c = 4.72 \text{ \AA}$, $\alpha = \beta = 90^\circ$, $\gamma = 120^\circ$), also results in a good fit to the experimental data for $x = 0.63$. These results indicate the discovery of Pnnm and/or P6₃/mmc nickel antimonate structures.

Identification of Stable Ordered Structures from Grand Potential Phase Diagram

Computational evaluation of the stability of the proposed Pnnm and P6₃/mmc prototypes is challenged by the mix of Ni, Sb, and vacancies on the cation sublattice. To perform density functional theory simulations, we identify the lowest energy ordered configurations of each

prototype as a representative phase of local crystallites in the experimental samples. Under the synthesis conditions of constant temperature and fixed oxygen partial pressure, the formation energy of a given $\text{Ni}_x\text{Sb}_{1-x}\text{O}_z$ phase is calculated by the grand potential energy,

$$\Delta E_f(\text{Ni}_x\text{Sb}_{1-x}\text{O}_z) = E(\text{Ni}_x\text{Sb}_{1-x}\text{O}_z) - x\mu_{\text{Ni}} - (1-x)\mu_{\text{Sb}} - z\mu_{\text{O}},$$

where μ is the chemical potential of the respective element. Chemical potentials of Ni and Sb are calculated such that the formation energy of the most stable unary metal oxide is set to zero, e.g., $\Delta E_f(\text{NiO}, \text{Sb}_2\text{O}_3) \equiv 0$ at $T = 700$ °C, and 0.2 atm O_2 . The oxygen chemical potential under experimental conditions is calculated as

$$\mu_{\text{O}} = \mu_{\text{O}}^{\circ}(T, P) + k_b T \ln(p/p^{\circ}),$$

where k_b is the Boltzmann constant, T is temperature, p is the oxygen partial pressure in atm, and p° is the reference pressure of 1 atm. The reference oxygen chemical potential, $\mu_{\text{O}}^{\circ}(T, P)$, was calculated relative to the experimental formation energy of water at 0 K and 1 atm,

$$\mu_{\text{O}}^{\circ}(0 \text{ K}, 1 \text{ atm}) = \Delta H_{\text{H}_2\text{O}}^{\text{DFT}}(0 \text{ K}, 1 \text{ atm}) - \frac{1}{2}\Delta H_{\text{H}_2}^{\text{DFT}}(0 \text{ K}, 1 \text{ atm}) - (-241.826 \text{ kJ/mol}).$$

Formation energies calculated from DFT include both electronic and zero-point-energy contributions. The temperature dependence of μ_{O}° is taken from experimental values^{24,25}.

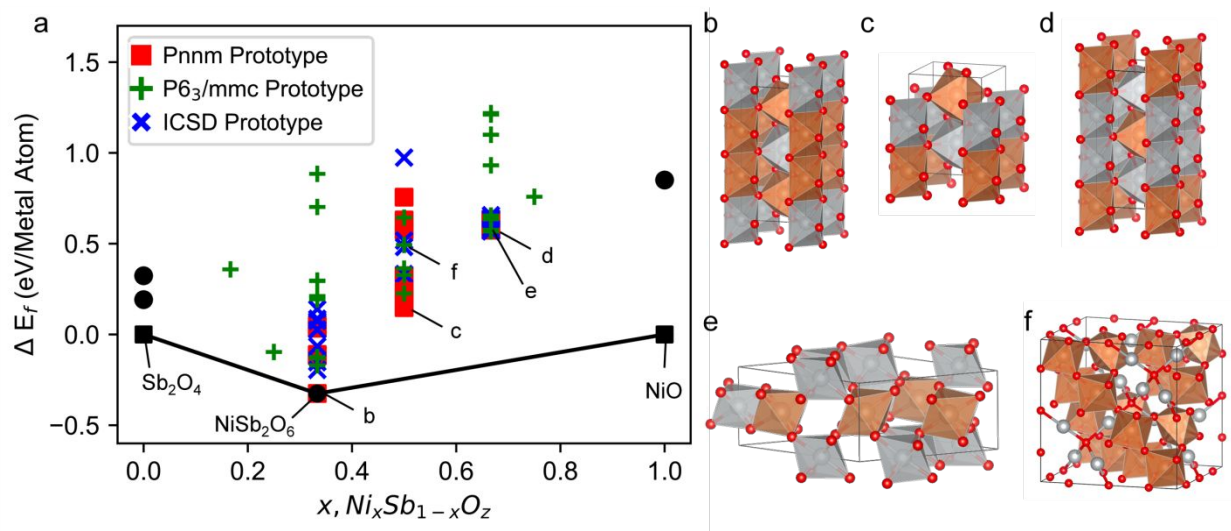


Figure 2: (a) Grand potential phase diagram comparing the formation energy, ΔE_f , at oxygen chemical potential of -5.79 eV (700 °C and 0.2 atm O_2) including discovered disordered Pnnm and $P6_3/mmc$ prototype structures. The convex hull connects the thermodynamically stable phases as a function of composition shown with the black line, with labeled compositions for the phases on the convex hull. The crystal structure of the most stable phase identified for each composition is (b) $x = 0.33$ R- $Ni_2Sb_4O_{12}$, (c) $x = 0.50$ R- $Ni_2Sb_2O_8$, (d)/(e) $x = 0.66$ R- $Ni_4Sb_2O_{12}$, and hex- $Ni_6Sb_3O_{18}$ respectively. (f) Structure of $Ni_4Sb_4O_{14}$ pyrochlore structure is used to determine the metastability limit, since this is an experimentally known phase that resides well above the DFT energy hull. Structures in (b, c, d, e, f) correspond to the labeled points in (a). For each crystal structure, Sb octahedra are orange, Ni atoms and octahedra are gray, and oxygen atoms are red.

We construct a one-dimensional phase diagram of the formation energy including many different ordered structures of the fitted disordered prototypes to identify the most stable structure at different Ni/Sb ratios. For the Pnnm prototype (Figure 1d) we consider orderings in a supercell of $(1 \times 1 \times 3)$ for $x = 0.33$ and $x = 0.66$ and $(1 \times 1 \times 2)$ for $x = 0.5$ which tests mixing along the c -axis. Additionally, we consider $(\sqrt{2} \times \sqrt{2} \times 2)$ supercell for $x = 0.5$ which allows for mixing along the ab -plane. Similarly, for the $P6_3/mmc$ space group prototype, we calculate the DFT-energy of $(3 \times 3 \times 1)$ ordered supercells for $x = 0.33$, 0.50 and 0.66 . For each supercell, the starting fractional occupation of all disorder-cation sites is identical and chosen to achieve an overall stoichiometry of Ni_xSb_{1-x} .

$x\text{O}_2$. Since these supercells do not have fractional site occupancy, their formal space group will be lower in symmetry than the structures of Figures 1c, d. However, assessing the stability of the supercells in the context of the Ni-Sb-O grand potential phase diagram will provide insights into the thermodynamics of the cation-disordered structures derived from experimental XRD patterns.

Calculating the energy of all combinations of ordered occupations for each structure would be infeasible (over 59 thousand orderings for the $x = 0.5$ disordered rutile structure alone), we therefore limit our search to the symmetrically distinct orderings within 1.5 eV/atom of the lowest predicted Ewald electrostatic energy.²¹ We also include in our preliminary structure survey additional structure prototypes from other known metal antimony oxides in the ICSD⁶ with appropriate Ni substitution for non-Sb cations. Phase stability for all phases was compared by calculating the grand potential formation energy (Figure 2) with a fixed oxygen chemical potential corresponding to the experimental annealing conditions of 0.2 atm O_2 and 700 °C. The structures used for DFT calculations are referred to with unit cell stoichiometries and integer subscripts, to differentiate them from the experimental and cation-disordered prototype compositions.

The predicted stable monometallic oxides under synthesis conditions are rutile antimony oxide, $\text{R-Sb}_2\text{O}_4$, and NiO which are consistent with the observed peaks in the XRD patterns for Sb and Ni rich phases respectively. The only stable mixed Ni-Sb-O phase on the convex hull is tri-rutile ($\text{R-Ni}_2\text{Sb}_4\text{O}_{12}$) at $x = 0.33$ and $\Delta E_f = -0.5$ eV / metal atom (Figure 2b). The DFT-optimized lattice parameters are $a = b = 4.72$ Å, $c = 9.36$ Å, which is within 2% of that calculated in the experimental XRD pattern. In this most stable configuration, there are two symmetrically equivalent Ni atoms with maximum dispersion and all oxygen atoms are symmetrically equivalent. The oxygens are

coordinated with two Sb atoms and one Ni such that along the c-axis there exists an equal number of Sb-Ni, Sb-Sb, and Ni-Ni edge shared octahedra. The local magnetic moment for Ni is $\sim 1.7 \mu_B$ with no net moment observed for either Sb or O corresponding to formal +2, +5 and -2 oxidation states. The calculated bandgap is 0.45 eV indicating a semiconductor; however, the magnitude of the bandgap is much less than experimental measurements of 1.6-2.83 eV^{26,27}. Additionally, the antiferromagnetic and ferromagnetic configurations are approximately the same energy and only differ by 0.003 eV / metal atom which is much more similar in energy than previous calculations of this phase⁴. These two apparent discrepancies (smaller bandgap and similar ferromagnetic and antiferromagnetic energies) are explained by the choice of the Hubbard U parameter for Ni ($U_{\text{eff}} = 3$), which was chosen to minimize the error in enthalpy of formation across nickel oxides with multiple oxidation states rather than bandgap (Figure S4) and is lower than that used in other works²⁸.

No other calculated structures for $x = 0.50$ or 0.66 lie on the convex hull and therefore predict the synthesized phases to be metastable. We estimate the metastability limit from a pyrochlore phase ($\text{Ni}_4\text{Sb}_4\text{O}_{14}$, mp-1190650), which has been experimentally synthesized (Figure 2f) under 0.2 atm O_2 and 450 °C annealing conditions²⁹. This pyrochlore phase is above the convex hull, with $\Delta E_{\text{hull, pyrochlore}} = 0.61$ eV / metal atom as calculated at its synthesis conditions. We therefore estimate the upper bound of metastability in the Ni-Sb-O phase based on the energetics of this pyrochlore structure, and any phase with $\Delta E_{\text{hull}} < 0.61$ eV / metal atom may be synthesizable. The pyrochlore structure is not a viable candidate for the observed phases in this study because of the dissimilarity between the calculated and observed XRD pattern.

For the $x = 0.5$ composition the lowest energy phase we could identify was a metastable bi-rutile ($\text{R-Ni}_2\text{Sb}_2\text{O}_8$) with $\Delta E_{\text{hull}} = 0.30$ eV/metal atom (Figure 2c). The metastable bi-rutile is a $(1 \times 1 \times 2)$ supercell of the rutile structure with stacking of alternating Ni and Sb edge shared octahedra along the c -axis. No magnetic moments are observed on either Sb or O, and the Ni magnetic moment is 1.1 indicating +5, -2, and +3 oxidation states of Sb, O and Ni, respectively. Antiferromagnetic and ferromagnetic configurations are approximately the same energy with $\Delta E_{\text{afm}} - \Delta E_{\text{fm}} = 0.002$ eV/metal atom. The calculated bandgap is 0.29 eV and is similar to that calculated for $x = 0.33$. Experimentally, $x = 0.33$ and $x = 0.5$ compositions also share similar bandgaps.

We identified two structures of similar formation energy for the Ni-rich, $x = 0.66$, phase. The most stable ordered structure of the Pnnm disordered prototype is tri-rutile ($\text{R-Ni}_4\text{Sb}_2\text{O}_{12}$) with $\Delta E_{\text{hull}} = 0.73$ eV/metal atom. Stacking along the c -axis occurs in a similar configuration to $x = 0.66$ with Sb and Ni atoms swapped (Figure 2d). In the unit cell, there are two magnetically distinct Ni atoms, one pair of edge sharing Ni octahedra has moments of $0.63 \mu_{\text{B}}$ and another pair of edge sharing Ni octahedra has moments $0.73 \mu_{\text{B}}$ which does not correspond to the formal Ni +3.5 oxidation state. Instead, slight magnetic moments on the oxygen are observed, indicating a more covalent and possibly less stable Ni-O bond in this Ni-rich configuration compared to either $x = 0.50$ or $x = 0.33$. The $\Delta E_{\text{hull}} = 0.72$ eV/metal atom is above the approximate metastability limit, and its DFT electronic structure is metallic, which does not align with the experimental observation of a similar band gap for all compositions $0.33 < x < 0.67$, motivating further refinement of the computational model for this phase in the following section.

The second phase identified for $x = 0.66$ is an ordered configuration of the $P6_3/mnc$ hexagonal prototype phase ($\text{hex-Ni}_6\text{Sb}_3\text{O}_{18}$). This hexagonal phase is composed of two layers of alternating Ni-rich and Sb-rich layers (Figure 2e) with an identical formation energy $\Delta E_{\text{hull}} = 0.72$ eV/metal atom which is also above the metastability limit. This configuration minimized the electrostatic Ewald electrostatic energy for the $x = 0.66$ composition and is in a space group found in other metal antimony oxides prototypes including $\text{Mn}(\text{SbO}_3)_2$ (mp-25043) and $\text{Hg}(\text{SbO}_3)_2$ (mp-754065). There are six Ni atoms in the unit cell with three distinct Ni magnetic moments: within the Ni rich layer there are three with $0.926 \mu_B$ (Ni^{+3}) and two with $0.09 \mu_B$ (Ni^{+4}), and $0.18 \mu_B$ (Ni^{+4}) in the Sb-rich layer. The magnetic moments do not correspond to formal oxidation states, instead indicating a more covalent and possibly less bonding character between the Ni and oxygen. This structure is ferromagnetic with an overall magnetic moment of $3 \mu_B$ and has a calculated bandgap of 0.30 eV which is nearly identical in magnitude to that calculated for both $x = 0.50$ and $x = 0.33$.

Having identified the most stable ordered-structures consistent with the identified disordered prototypes and XRD patterns, we calculate the XAS spectra for further comparison of the Ni oxidation states with experiments.

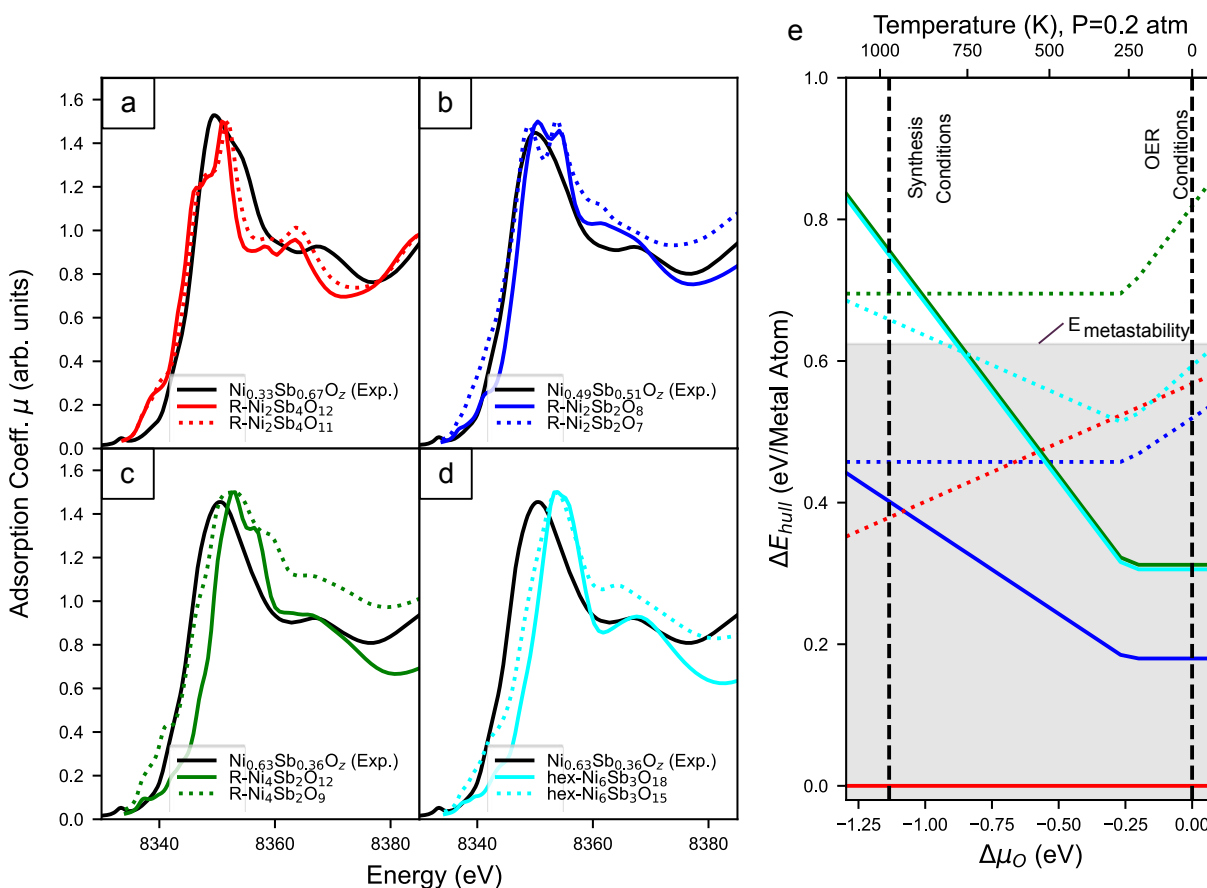


Figure 3: (a-d) XAS Ni K-edge comparisons for $\text{Ni}_x\text{Sb}_{1-x}\text{O}_z$ for (a) $x = 0.33$, (b) $x = 0.50$, and (c, d) $x = 0.66$. Experimental spectrum for each composition is shown with a solid black line. Simulated spectra are shown in color for the calculated rutile (a, b, c) and hexagonal (d) structures. Solid colored lines represent calculated structures with no oxygen vacancies ($z = 2$). Dotted lines represent calculated structures with most-stable oxygen vacancies ($z < 2$), which generally shift the Ni K-edge to lower energies. (e) The energy above hull (ΔE_{hull}) of each calculated structure as a function of relative oxygen chemical potential ($\Delta\mu_{\text{O}}$). The color and line style correspond to the same calculated structure as in (a-d). Vertical dashed lines mark the reducing synthesis and oxidizing OER measurement conditions. The metastability limit (shaded gray region) is defined as the ΔE_{hull} for pyrochlore- $\text{Ni}_2\text{Sb}_2\text{O}_7$ at 0.2 atm O_2 and 450°C. Under synthesis conditions, oxygen vacancies have a positive formation energy for $x = 0.33$ and 0.50, and a negative formation energy for $x = 0.66$. Under OER conditions, oxygen vacancies are unstable at all Ni concentrations.

Stability of Oxygen Vacancies and effect on Ni XAS Spectra

Using the synthesized thin films with $x = 0.33, 0.49, \text{ and } 0.63$, Ni K edge spectra were acquired and found to not vary considerably despite the substantial differences in composition and phase (Figure 3a-3d, solid black lines, plotted together in Figure S5). By comparing the K-edge positions to reference NiO and NiOOH spectra, the Ni oxidation state is estimated to be +2.5 for all Ni/Sb ratios. However, the compositions of the identified phases from our grand potential diagram for $x = 0.33, 0.50, 0.66$ are $\text{Ni}_2\text{Sb}_4\text{O}_6$, $\text{Ni}_2\text{Sb}_2\text{O}_8$, $\text{Ni}_4\text{Sb}_2\text{O}_{12}$ which have formal Ni oxidation states of +2, +3, and +3.5 respectively. For $x = 0.33$, Ni is formally more reduced than measured, and in $x = 0.50$ and 0.66 Ni are more oxidized than measured. The simulated Ni K edge spectra of these oxidized phases (Figure 3a-3d, solid-colored lines) has increasing edge energy with increasing formal oxidation state, causing a discrepancy between the measured and simulated spectra that increases with increasing Ni concentration.

To address this discrepancy, we consider the effect of oxygen vacancies on the Ni oxidation state and evaluate their thermodynamic stability. The formation energy for oxygen vacancies, $\Delta E_{form}^{O Vac}$, as a function of oxygen chemical potential for a given structure relative to the fully oxidized structure is,

$$\Delta E_{form}^{O Vac} = E(\text{Ni}_x\text{Sb}_{1-x}\text{O}_{z-n}) - E(\text{Ni}_x\text{Sb}_{1-x}\text{O}_z) + n\mu_O = \Delta E_{hull}(\text{Ni}_x\text{Sb}_{1-x}\text{O}_{z-n}) - \Delta E_{hull}(\text{Ni}_x\text{Sb}_{1-x}\text{O}_z)$$

where n is the stoichiometric number of oxygens removed from the simulated cell. We consider $n = 1$ for $x = 0.33$ (R- $\text{Ni}_2\text{Sb}_4\text{O}_{12-n}$), $n = 1, 2, 3$ for $x = 0.5$ (R- $\text{Ni}_2\text{Sb}_2\text{O}_{8-n}$), and $n = 1, 2, 3, 4$ for $x = 0.66$ (R- $\text{Ni}_4\text{Sb}_2\text{O}_{12-n}$ and hex- $\text{Ni}_6\text{Sb}_3\text{O}_{18-n}$). Similar to our approach for calculating cation occupation geometries, we limit the search space for possible configurations with multiple

vacancies by only performing a DFT relaxation on the symmetrically distinct structures within 1.5 eV/metal atom of the lowest predicted Ewald electrostatic energy for that stoichiometry.

The formation energy of a single oxygen vacancy for $x = 0.33$ (R-Ni₂Sb₄O₁₁) is very large at 0.39 eV/metal atom and is unfavorable even under very reducing experimental conditions. The presence of the oxygen vacancy did not change the Ni magnetic moment (1.7 μ_B) compared to the fully oxidized composition and did not impact the simulated XAS spectra with both in reasonable agreement with the experimental spectra (Figure 3a). Even though the formation energy of R-Ni₂Sb₄O₁₁ is within the metastability limit (Figure 3e red dashed line), we do not expect any oxygen vacancies to form for $x = 0.33$ due to the large driving force to completely oxidize to R-Ni₂Sb₄O₁₂ (Figure 3e solid red line).

For $x = 0.50$, there are two symmetrically distinct oxygen atoms. The first is 2-coordinated with Ni (single coordination with Sb) and the second is singly coordinated with Ni (2-coordination with Sb). The 2-Ni-coordinated oxygen is more weakly bonded and thus exhibits the lower vacancy formation energy of $\Delta E_{form}^{O Vac} = 0.06$ eV/metal atom. Introducing a single oxygen atom vacancy changes the magnetic moment on both Ni atoms to 1.7 μ_B and lowers Ni oxidation as reflected in the simulated XAS spectra (Figure 3b) with the edge of R-Ni₄Sb₄O₇ shifting to lower energy and in good alignment with the experimental data. Further reducing the system and creating a second oxygen vacancy (R-Ni₄Sb₄O₆) is more unfavorable with $\Delta E_{form}^{O Vac} = 0.24$ eV/metal atom and introduces additional peaks along the simulated K-edge inconsistent with the experimental spectra (Figure S6). The overall formation energies of both the reduced R-Ni₄Sb₄O₇ and oxidized

R-Ni₄Sb₄O₈ structures are within the metastability limit and may co-exist under synthesis conditions (Figure 3e solid and dashed blue lines).

The Ni-rich $x = 0.66$ composition is most easily reduced and stabilized by the presence of oxygen vacancies. Starting from R-Ni₄Sb₂O_{12-n}, sequentially introducing oxygen vacancies is energetically favorable for $n = 1, 2, 3$ with $\Delta E_{form}^{O Vac}$ of -0.02, -0.03, and -0.05 eV / metal atom respectively. Three oxygen vacancies (R-Ni₄Sb₂O₉) resulted in the lowest energy configuration with $\Delta E_{hull} = 0.65$ eV / metal atom (Figure 3e, green-dashed line), and the shift of formal oxidation state to Ni⁺² is reflected in the low Ni K edge energy (Figure 3c). Similarly for hex-Ni₆Sb₃O_{18-n}, the first three oxygen vacancies are thermodynamically favorable with hex-Ni₆Sb₃O₁₅ found as the most stable with $\Delta E_{form}^{O Vac} = -0.1$ eV/metal atom and $\Delta E_{hull} = 0.62$ eV/metal atom (Figure 3e, cyan-dashed line). At this composition, half the Ni atoms in the unit cell are +3 with magnetic moments of 1.63 μ_B and half are +2 with magnetic moments of 0.9 μ_B . For both R-Ni₄Sb₂O₁₂ and hex-Ni₆Sb₃O₁₈, introduction of oxygen vacancies resulted in similar hull energies, and shifted the simulated Ni-K edge to lower energies in better alignment with the experimental spectra. While the most energetically stable stoichiometry we identified for $x = 0.66$ is hex-Ni₆Sb₃O₁₅, it is possible that alternate or larger supercell vacancy configurations may exhibit lower formation energies.

In total, the computational structures best supported by XRD and XAS experiments are R-Ni₂Sb₄O₁₂, R-Ni₂Sb₂O₇, hex-Ni₆Sb₃O₁₅ and R-Ni₄Sb₂O₉, with a propensity for oxygen vacancy formation that increases with increasing Ni concentration. While oxygen vacancies may be kinetically stabilized after synthesis, their unfavorable energetics under OER conditions (Figure

3e) suggest that near-surface oxygen vacancies will be filled during electrochemical operation, motivating the study of vacancy-free structures for studying OER catalysis and Pourbaix energetics.

Identification of OER Surface Coverage

We first identify the relevant surface coverages on multiple surface facets for each composition and consider the activity on the standard rutile (101) and (110) surfaces for each of the three compositions, and on the (100) surface for the hex- $\text{Ni}_6\text{Sb}_3\text{O}_{18}$. On both the (101) and (110) surfaces we consider two types of active oxygen sites: single coordinated on-top sites on either a Ni ($\text{O}_{1c}\text{-N}$) or Sb atom ($\text{O}_{1c}\text{-S}$) and double coordinated (O_{2c}) bridge sites which have not been extensively investigated in these systems (Figure 4). The types of bridge site differ between each of the compositions, either between two Ni atoms ($\text{O}_{2c}\text{-NN}$), two Sb atoms ($\text{O}_{2c}\text{-SS}$), or a Ni-Sb bridge

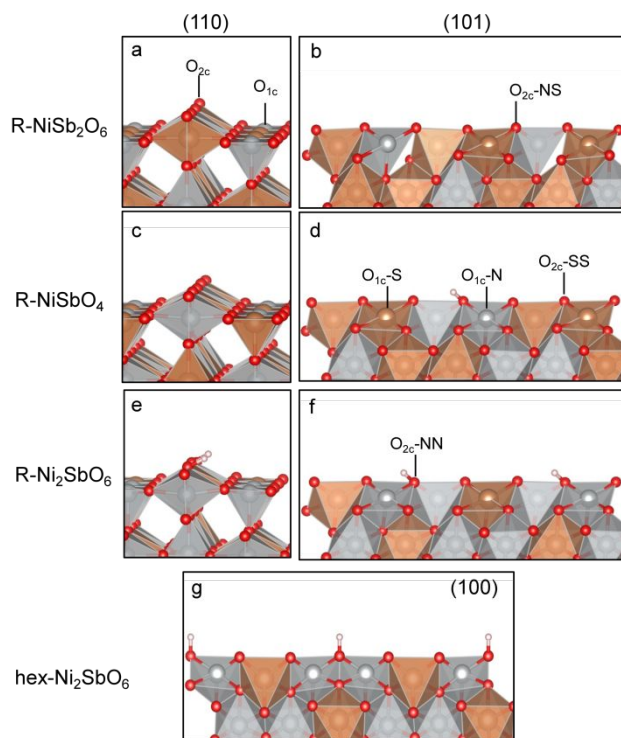


Figure 4: Most common surface under reaction conditions for (a, b) $\text{R-Ni}_4\text{Sb}_2\text{O}_{12}$, (c, d) $\text{R-Ni}_3\text{Sb}_3\text{O}_{12}$, (e, f) $\text{R-Ni}_4\text{Sb}_2\text{O}_{12}$, and (g) $\text{hex-Ni}_6\text{Sb}_3\text{O}_{18}$. (a, c, e) show (110) surface terminations, (b, d, f) show (101) surfaces, and (g) is the (100) surface. The bridge O_{2c} sites are most catalytically active (see Figure 5), while the top- O_{1c} sites are empty and only activated under much higher potentials not realized during OER experiments. Surface Pourbaix diagrams for all surfaces and compositions given in Fig S7.

(O_{2c}-NS). The most stable surface terminations for each of the available oxygen sites under reaction conditions were determined by sequentially oxidizing each active site and calculating the surface Pourbaix Diagram (Figure S7).

The most active surfaces on both (110) and (101) surfaces for all compositions included vacant top sites (Figures 4a-g), with the differences between various Ni compositions arising solely from the terminations of the different bridge sites. Both O_{2c}-NS and O_{2c}-SS bridge sites on $x = 0.33$ (110) and (101) surfaces are all oxygen terminated, with nickel remaining in the +2 oxidation state (Figure 4 a,b). Similarly for R-Ni₂Sb₂O₈ ($x = 0.5$), the (101) O_{2c}-NS site, and (110) O_{2c}-SS, and O_{2c}-NS sites are oxygen terminated (Figure 4c,d). However, on the (101) surface there is an additional OH terminated O_{2c}-NN site with the additional charge compensated equally between the two nickel atoms (Figure 4d). We also note that the Ni₂Sb₂O₈ (110) primitive surface has two symmetrically distinct sites for each O_{2c}-NS and O_{1c}-N. For $x = 0.66$, on the (110) surface, the O_{2c}-NN site is most easily oxidized, and O terminated under OER conditions, and the remaining O_{2c}-NS bridge site is the most active and predicted to be OH terminated (Figure 4e). An identical trend is observed on the (110) surface: O_{2c}-NS oxygen terminated, and O_{2c}-NN are OH terminated (Figure 4e). For hex-Ni₆Sb₃O₁₈, we only considered the (100) termination corresponding to the most prevalent peak in the observed XRD pattern (Figure 1b, green line) and find its termination very similar to the rutile configuration with oxygen at the O_{2c}-NS sites, and OH at the O_{2c}-NN site (Figure 4g).

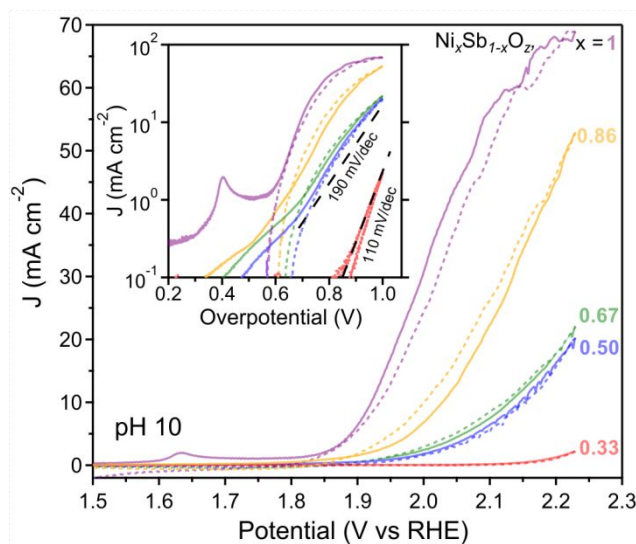


Figure 5: Experimental evaluation of OER activity in pH 10 borate-buffered electrolyte. The five as-synthesized compositions are labelled by their respective Ni concentration, x , with each initial (anodic) sweep shown as a solid line and the subsequent (cathodic) sweep shown as a dotted line. The inset shows the portion of each CV with current density above 0.1 mA cm^{-2} on a logarithmic scale, with dashed black lines showing characteristic Tafel slopes.

The Measured and Calculated OER Overpotentials

Experimental evaluation of OER activity was carried out in pH 10 electrolyte on a series of 4 $\text{Ni}_x\text{Sb}_{1-x}\text{O}_z$ compositions annealed at 700°C as well as a Ni-O electrode ($x = 1$) annealed at 610°C . Cyclic voltammograms (CVs) are shown in Figure 5, revealing substantial compositional variation in activity with $x = 0.33$ showing the lowest activity but also lowest apparent Tafel slope, approximately 110 mV dec^{-1} . The Tafel slopes of the more Ni-rich samples are less well-defined and are generally larger, up to 190 mV dec^{-1} . The overpotential at a current density of 10 mA cm^{-2} is used as an activity descriptor, which for the $x = 0.33$ sample requires an extrapolation as shown in the inset of Figure 5. Additional photoelectrochemical characterization (Figure S9) and TEM

To further understand the OER activity of these systems, we calculate and plot the two main binding energy descriptors for each site on the active surface termination shown in Figure 4, ΔG_{*OH} , and $\Delta G_{*O} - \Delta G_{*OH}$, and the associated activity volcano (Figure 6a, individual data points given in Table S2) based on a fitted scaling relationship between ΔG_{*OOH} and ΔG_{*OH} (Figure S8). Some general trends among the adsorption energies across types of active sites, surfaces, and composition are observed. Firstly, the activity of the top sites is generally limited by the unfavorable binding energy of $*OH$ and are clustered in the top right corner of Figure 6a and are not very active with overpotentials $> 0.8V$ and rate limiting steps of $*OH \rightarrow *O$ or $* \rightarrow *OH$. The active bridge sites all have intermediate binding energies of $*OH$ following the binding strength trend $Sb-O-Sb > Sb-O-Ni > Ni-O-Ni$, and with associated differences in activity resulting from different $*O$ binding energies. The same site is generally more active on the (101) surface than the (110) surface with both weaker $*OH$ bonding, and weaker $*O$ binding. This trend is explained by the higher surface energy for (101) compared to (110) which increases the ability of the cations to participate in the catalytic process. The bridge sites for $Ni_2Sb_4O_{12}$ are all limited by the $*O \rightarrow *OOH$ step (stronger adsorption, left side of Figure 6a), whereas the limiting reaction is $*OH \rightarrow *O$ on the $Ni_2Sb_2O_8$ and $Ni_4Sb_2O_{12}$ surfaces (weaker adsorption, right side of Figure 6a). None of the sites considered had the final deprotonation and desorption step ($*OOH \rightarrow O_2$) rate as limiting. Our calculated overpotentials, based on single site mechanism via OOH^* , serve as upper bound for the activity and considering recently proposed alternatives such as direct O-O coupling³⁰ or OOH^* dual site stabilization³¹ would further lower these values.

There is good qualitative agreement with the calculated overpotentials as a function of composition compared to experimental measured values (Figures 5 and 6b). The lowest calculated overpotential decreases with increasing Ni concentration from 0.80 to 0.51 to 0.49 V at $x = 0.33$, 0.50, and 0.66 respectively. The relative trend of increasing Ni resulting in lower over potential is also observed experimentally. Discrepancies between the exact calculated overpotential and the experimental values are to be expected because in the real catalyst there will be a distribution of active sites, and the kinetics of stability/corrosion of each of the sites is not considered. The closest calculated overpotentials to the experimental values are the (101) O_{1c} -N for $Ni_2Sb_4O_{12}$, (101) O_{1c} -N for $Ni_2Sb_2O_8$, and (101) O_{2c} -NN for $Ni_4Sb_2O_{12}$.

In the $x = 1$ limit, we considered both NiO_2 (200), and NiO (111) surfaces which have calculated overpotentials significantly higher than experiments (Figure 6b) likely due to adventitious Fe incorporation from the electrolyte.³² Experimentally, the Ni-Sb films have higher overpotential, suggesting that Fe-based modification of the OER activity is less prevalent in the nickel antimonates than in $NiOOH$ -based catalysts.

energies are less than the 1 eV/atom (i.e., within the possible systematic errors from ion reference energies) indicating sufficiently low driving force towards corrosion and general stability at operating conditions.³ R-Ni₂Sb₄O₁₂ appears as a stable phase on the Pourbaix hull because it is also on the grand potential phase diagram convex hull in Figure 2a. The predicted decomposition products under reaction conditions for both $x = 0.5$ and $x = 0.66$ are R-NiSb₂O₆ and NiO₂. The above bulk thermodynamics indicate any Ni-rich phase may self-passivate with a kinetically stabilized R-NiSb₂O₆ layer in neutral to acidic OER conditions. The specific mechanism of passivation has not been investigated but may occur through the dissolution of a soluble intermediate that precipitates on the surface similar to other anode passivation mechanisms.³⁴ In pH 10 electrolyte, R-NiSb₂O₆ is thermodynamically stable under OER conditions and remains stable down to approximately 0.2 V vs SHE where corrosion is predicted to occur with a decomposition into Ni⁺²_(aq) and SbOH_{2(aq)}. The same cathodic corrosion reaction is predicted to occur for R-Ni₂Sb₂O₈ and R-Ni₄Sb₂O₁₂ at the same potential and pH. The combination of favorable Pourbaix energetics over a wide potential range and the availability of Pourbaix-stable passivation layers makes the entire family of nickel antimonates suitable for operationally-stable OER catalyst.

Conclusions

In this work we integrate theory and experiment to provide a comprehensive study of the phase behavior, OER activity, and Pourbaix stability in the Ni-Sb-O system. Motivated by the discovery of a new family of crystal structures via combinatorial experimentation, we performed a computational structure search, identifying the new phases as disordered rutile and layered

structures. To establish periodic structures that enable DFT studies, the most stable Ni-Sb orderings on the cation sublattice are identified. These structures include three rutile-like geometries and one hexagonal-layered structure, which provide the bases for a computational evaluation of phase behavior in the Ni-Sb-O system. Evaluation of the formation energy for oxygen vacancies and comparison with experimental XAS Ni spectra reveal the increased propensity for oxygen vacancies with increasing Ni concentration.

By addressing a broad range of candidate active sites, the composition dependent OER overpotential was found to decrease with increasing Ni concentration, in concert with combinatorial electrochemical characterization of OER activity. The active site was determined to be a O_{2c} -bridge sites rather than the metal on-top sites considered in prior work. The electrochemical stability of each of the three phases was calculated based on the Pourbaix analysis, and the ΔG_{pbx} was < 1 eV for all phases and availability of solid-state passivation layers support the experimental observation of excellent operational stability. The computational identification of the new phases in the Ni-Sb-O system also reveal similar energetics for a range of local atomic configurations, which elucidates the high crystallization temperature of nickel antimonates due to the mild thermodynamic driving forces for establishing long-range order. This combined theory-experiment approach demonstrates how foundational understanding of amorphous materials can be obtained via consideration of a range of computational structures, and the combination of OER activity and Pourbaix stability of the nickel antimonates further establish their promise for applications in solar fuels and beyond.

Author Contributions

K.R. performed calculations under supervision of M.B.. L.Z. synthesized and characterized materials with Y.Lai contributing electrochemical and M.R. contributing TEM analysis. X.L. and Y.Lu performed x-ray absorption spectroscopy measurements under supervision of J.Y.. J.G. and M.B. supervised the research and coordinated the experimental and computational effort. The manuscript was written by K.R. and L.Z. with contributions from J.G. and M.B. using data from all authors. All authors have given approval to the final version of the manuscript.

Notes

The authors declare no competing conflicts of interest, financial or otherwise. All atomic configurations and DFT calculated energies are available in CatalysisHub³⁵ at <https://www.catalysis-hub.org/publications/RaoResolving2022>.

Acknowledgements

This material is based on work performed by the Liquid Sunlight Alliance, which is supported by the U.S. Department of Energy, Office of Science, Office of Basic Energy Sciences, Fuels from Sunlight Hub under Award DE-SC0021266. XAS data collection (BL 9-3 and 7-3) was carried out at Stanford Synchrotron Radiation Lightsource, SLAC National Accelerator Laboratory, supported by the U.S. Department of Energy, Office of Science, Office of Basic Energy Sciences under Contract DE-AC02-76SF00515. Computational resources were provided by the National Energy Research Scientific Computing Center, a DOE Office of Science User Facility supported

by the Office of Science of the U.S. Department of Energy under Contract No. DE-AC02-05CH11231.

References

- (1) Xu, S.; Carter, E. A. Theoretical Insights into Heterogeneous (Photo)Electrochemical CO₂ Reduction. *Chem. Rev.* **2019**, *119*(11), 6631–6669. <https://doi.org/10.1021/acs.chemrev.8b00481>.
- (2) Liu, Y.; Guo, L. On Factors Limiting the Performance of Photoelectrochemical CO₂ Reduction. *J. Chem. Phys.* **2020**, *152*(10), 100901. <https://doi.org/10.1063/1.5141390>.
- (3) Rao, K. K.; Lai, Y.; Zhou, L.; Haber, J. A.; Bajdich, M.; Gregoire, J. M. Overcoming Hurdles in Oxygen Evolution Catalyst Discovery via Codesign. *Chem. Mater.* **2022**, *34*(3), 899–910. <https://doi.org/10.1021/acs.chemmater.1c04120>.
- (4) Zhou, L.; Peterson, E. A.; Rao, K. K.; Lu, Y.; Li, X.; Lai, Y.; Bauers, S. R.; Richter, M. H.; Kan, K.; Wang, Y.; Newhouse, P. F.; Yano, J.; Neaton, J. B.; Bajdich, M.; Gregoire, J. M. Addressing Solar Photochemistry Durability with an Amorphous Nickel Antimonate Photoanode. *Cell Reports Physical Science* **2022**, *3*(7), 100959. <https://doi.org/10.1016/j.xcrp.2022.100959>.
- (5) Mavračić, J.; Mocanu, F. C.; Deringer, V. L.; Csányi, G.; Elliott, S. R. Similarity Between Amorphous and Crystalline Phases: The Case of TiO₂. *J. Phys. Chem. Lett.* **2018**, *9*(11), 2985–2990. <https://doi.org/10.1021/acs.jpcclett.8b01067>.
- (6) Gunasooriya, G. T. K. K.; Nørskov, J. K. Analysis of Acid-Stable and Active Oxides for the Oxygen Evolution Reaction. *ACS Energy Lett.* **2020**, *5*(12), 3778–3787. <https://doi.org/10.1021/acsenergylett.0c02030>.
- (7) Gunasooriya, G. T. K. K.; Kreider, M. E.; Liu, Y.; Zamora Zeledón, J. A.; Wang, Z.; Valle, E.; Yang, A.-C.; Gallo, A.; Sinclair, R.; Stevens, M. B.; Jaramillo, T. F.; Nørskov, J. K. First-Row Transition Metal Antimonates for the Oxygen Reduction Reaction. *ACS Nano* **2022**, *16*(4), 6334–6348. <https://doi.org/10.1021/acsnano.2c00420>.
- (8) Moreno-Hernandez, I. A.; MacFarland, C. A.; Read, C. G.; Papadantonakis, K. M.; Brunshwig, B. S.; Lewis, N. S. Crystalline Nickel Manganese Antimonate as a Stable

- Water-Oxidation Catalyst in Aqueous 1.0 M H₂SO₄. *Energy Environ. Sci.* **2017**, *10*(10), 2103–2108. <https://doi.org/10.1039/C7EE01486D>.
- (9) Evans, T. A.; Choi, K.-S. Electrochemical Synthesis and Investigation of Stoichiometric, Phase - Pure CoSb₂O₆ and MnSb₂O₆ Electrodes for the Oxygen Evolution Reaction in Acidic Media. *ACS Appl. Energy Mater.* **2020**, *3*(6), 5563–5571. <https://doi.org/10.1021/acsaem.0c00526>.
- (10) Zhou, L.; Shinde, A.; Montoya, J. H.; Singh, A.; Gul, S.; Yano, J.; Ye, Y.; Crumlin, E. J.; Richter, M. H.; Cooper, J. K.; Stein, H. S.; Haber, J. A.; Persson, K. A.; Gregoire, J. M. Rutile Alloys in the Mn–Sb–O System Stabilize Mn³⁺ To Enable Oxygen Evolution in Strong Acid. *ACS Catal.* **2018**, *8*(12), 10938–10948. <https://doi.org/10.1021/acscatal.8b02689>.
- (11) Gregoire, J. M.; Xiang, C.; Liu, X.; Marcin, M.; Jin, J. Scanning Droplet Cell for High Throughput Electrochemical and Photoelectrochemical Measurements. *Review of Scientific Instruments* **2013**, *84*(2), 024102. <https://doi.org/10.1063/1.4790419>.
- (12) Kresse, G.; Furthmüller, J. Efficiency of *Ab-Initio* Total Energy Calculations for Metals and Semiconductors Using a Plane-Wave Basis Set. *Computational Materials Science* **1996**, *6*(1), 15–50. [https://doi.org/10.1016/0927-0256\(96\)00008-0](https://doi.org/10.1016/0927-0256(96)00008-0).
- (13) Kresse, G.; Furthmüller, J. Efficient Iterative Schemes for *Ab Initio* Total-Energy Calculations Using a Plane-Wave Basis Set. *Phys. Rev. B* **1996**, *54*(16), 11169–11186. <https://doi.org/10.1103/PhysRevB.54.11169>.
- (14) Dudarev, S. L.; Botton, G. A.; Savrasov, S. Y.; Humphreys, C. J.; Sutton, A. P. Electron-Energy-Loss Spectra and the Structural Stability of Nickel Oxide: An LSDA+U Study. *Phys. Rev. B* **1998**, *57*(3), 1505–1509. <https://doi.org/10.1103/PhysRevB.57.1505>.
- (15) Perdew, J. P.; Burke, K.; Ernzerhof, M. Generalized Gradient Approximation Made Simple. *Phys. Rev. Lett.* **1996**, *77*(18), 3865–3868. <https://doi.org/10.1103/PhysRevLett.77.3865>.
- (16) Rehr, J. J.; Kas, J. J.; Vila, F. D.; Prange, M. P.; Jorissen, K. Parameter-Free Calculations of X-Ray Spectra with FEFF9. *Phys. Chem. Chem. Phys.* **2010**, *12*(21), 5503. <https://doi.org/10.1039/b926434e>.
- (17) Zheng, C.; Mathew, K.; Chen, C.; Chen, Y.; Tang, H.; Dozier, A.; Kas, J. J.; Vila, F. D.; Rehr, J. J.; Piper, L. F. J.; Persson, K. A.; Ong, S. P. Automated Generation and Ensemble-

- Learned Matching of X-Ray Absorption Spectra. *npj Comput Mater* **2018**, *4*(1), 12.
<https://doi.org/10.1038/s41524-018-0067-x>.
- (18) Nørskov, J. K.; Rossmeisl, J.; Logadottir, A.; Lindqvist, L.; Kitchin, J. R.; Bligaard, T.; Jónsson, H. Origin of the Overpotential for Oxygen Reduction at a Fuel-Cell Cathode. *J. Phys. Chem. B* **2004**, *108*(46), 17886–17892. <https://doi.org/10.1021/jp047349j>.
- (19) Hansen, H. A.; Rossmeisl, J.; Nørskov, J. K. Surface Pourbaix Diagrams and Oxygen Reduction Activity of Pt, Ag and Ni(111) Surfaces Studied by DFT. *Phys. Chem. Chem. Phys.* **2008**, *10*(25), 3722. <https://doi.org/10.1039/b803956a>.
- (20) Jain, A.; Ong, S. P.; Hautier, G.; Chen, W.; Richards, W. D.; Dacek, S.; Cholia, S.; Gunter, D.; Skinner, D.; Ceder, G.; Persson, K. A. Commentary: The Materials Project: A Materials Genome Approach to Accelerating Materials Innovation. *APL Materials* **2013**, *1*(1), 011002. <https://doi.org/10.1063/1.4812323>.
- (21) Ong, S. P.; Richards, W. D.; Jain, A.; Hautier, G.; Kocher, M.; Cholia, S.; Gunter, D.; Chevrier, V. L.; Persson, K. A.; Ceder, G. Python Materials Genomics (Pymatgen): A Robust, Open-Source Python Library for Materials Analysis. *Computational Materials Science* **2013**, *68*, 314–319. <https://doi.org/10.1016/j.commatsci.2012.10.028>.
- (22) Gregoire, J. M.; Dale, D.; Kazimirov, A.; DiSalvo, F. J.; van Dover, R. B. High Energy X-Ray Diffraction/x-Ray Fluorescence Spectroscopy for High-Throughput Analysis of Composition Spread Thin Films. *Review of Scientific Instruments* **2009**, *80*(12), 123905. <https://doi.org/10.1063/1.3274179>.
- (23) Dmitrienko, V. E. Anisotropy of X-Ray Susceptibility and Bragg Reflections in Cubic Crystals. *Acta Crystallogr A Found Crystallogr* **1984**, *40*(2), 89–95.
<https://doi.org/10.1107/S0108767384000209>.
- (24) Thomas C. Allison. NIST-JANAF Thermochemical Tables - SRD 13, 2013.
<https://doi.org/10.18434/T42S31>.
- (25) Reuter, K.; Scheffler, M. Composition, Structure, and Stability of RuO₂ (110) as a Function of Oxygen Pressure. *Phys. Rev. B* **2001**, *65*(3), 035406.
<https://doi.org/10.1103/PhysRevB.65.035406>.
- (26) Papi, N.; Hakimiyfard, A.; Tahmasebi, N.; Samimifar, M. Photocatalytic Degradation of Water Pollutant Dye by Solid State Synthesized Ni_{1-x}Ln_xSb₂O₆ (Ln=Eu, Gd, Ho and Yb) Nanocomposites. **2020**, 15.

- (27) Arunkumar, N.; Naraginti, S. Facile Synthesis of Nanostructured Trirutile Antimonates $M(II)Sb_2O_6$ ($M = Co, Cu, Ni, Fe$) and Its Visible Photocatalytic Studies. *Inorganic and Nano-Metal Chemistry* **2020**, 1–10. <https://doi.org/10.1080/24701556.2020.1866605>.
- (28) Wang, M. Enthalpy of Formation of $LiNiO_2$, $LiCoO_2$ and Their Solid Solution, $LiNi_{1-x}Co_xO_2$. *Solid State Ionics* **2004**, 166(1–2), 167–173. <https://doi.org/10.1016/j.ssi.2003.11.004>.
- (29) Zhou, H. D.; Wiebe, C. R.; Janik, J. A.; Vogt, B.; Harter, A.; Dalal, N. S.; Gardner, J. S. Spin Glass Transitions in the Absence of Chemical Disorder for the Pyrochlores $A_2Sb_2O_7$ ($A=Mn, Co, Ni$). *Journal of Solid State Chemistry* **2010**, 183(4), 890–894. <https://doi.org/10.1016/j.jssc.2010.01.025>.
- (30) Rao, R. R.; Corby, S.; Bucci, A.; García-Tecedor, M.; Mesa, C. A.; Rossmeis, J.; Giménez, S.; Lloret-Fillol, J.; Stephens, I. E. L.; Durrant, J. R. Spectroelectrochemical Analysis of the Water Oxidation Mechanism on Doped Nickel Oxides. *J. Am. Chem. Soc.* **2022**, 144(17), 7622–7633. <https://doi.org/10.1021/jacs.1c08152>.
- (31) Du, K.; Zhang, L.; Shan, J.; Guo, J.; Mao, J.; Yang, C.-C.; Wang, C.-H.; Hu, Z.; Ling, T. Interface Engineering Breaks Both Stability and Activity Limits of RuO_2 for Sustainable Water Oxidation. *Nat Commun* **2022**, 13(1), 5448. <https://doi.org/10.1038/s41467-022-33150-x>.
- (32) Burke, M. S.; Enman, L. J.; Batchellor, A. S.; Zou, S.; Boettcher, S. W. Oxygen Evolution Reaction Electrocatalysis on Transition Metal Oxides and (Oxy)Hydroxides: Activity Trends and Design Principles. *Chem. Mater.* **2015**, 27(22), 7549–7558. <https://doi.org/10.1021/acs.chemmater.5b03148>.
- (33) Singh, A. K.; Zhou, L.; Shinde, A.; Suram, S. K.; Montoya, J. H.; Winston, D.; Gregoire, J. M.; Persson, K. A. Electrochemical Stability of Metastable Materials. *Chem. Mater.* **2017**, 29(23), 10159–10167. <https://doi.org/10.1021/acs.chemmater.7b03980>.
- (34) Bockelmann, M.; Reining, L.; Kunz, U.; Turek, T. Electrochemical Characterization and Mathematical Modeling of Zinc Passivation in Alkaline Solutions: A Review. *Electrochimica Acta* **2017**, 237, 276–298. <https://doi.org/10.1016/j.electacta.2017.03.143>.
- (35) Winther, K. T.; Hoffmann, M. J.; Boes, J. R.; Mamun, O.; Bajdich, M.; Bligaard, T. Catalysis-Hub.Org, an Open Electronic Structure Database for Surface Reactions. *Sci Data* **2019**, 6(1), 75. <https://doi.org/10.1038/s41597-019-0081-y>.